Journal of Engineering Mathematics **25**: 329–352, 1991.

Secondary separation from a slender wing

K. KIRKKOPRU and N. RILEY*

*School of Mathematics, University of East Anglia, Norwich, UK (*author for correspondence)*

Received 2 November 1990; accepted 9 November 1990

Abstract. We consider the high Reynolds number laminar flow of an incompressible fluid past a slender delta wing at incidence. The primary separation is represented by vortex sheets emanating from the leading edges. These sheets also carry a source distribution to represent viscous displacement effects. An interactive viscous-inviscid calculation is carried out to determine the secondary-separation flow properties on the wing. Agreement between the theoretical predictions and experiment is encouraging. For example, unlike the purely inviscid calculations, there is only a small pressure recovery beyond the suction peak, as is observed in experiment. Similarly the upward and inboard movement of the vortex core due to the secondary separation is in accord with experiment, as is the position of secondary separation.

1. Introduction

Separation from the leading edges of a slender wing is a phenomenon that has been extensively explored. In particular there are several successful inviscid models available for it, the first of which is due to Smith [1]. In this model the flow separation is represented by spiral vortex sheets which spring from the leading edges of the wing, embedded within a potential flow. This vortex configuration results in an adverse pressure gradient for the flow over the wing surface, and promotes a viscous separation on the wing. We refer to the separation from the leading edge as the primary separation, the viscous boundary-layer separation on the wing surface as the secondary separation.

Experiments, for example by Marsden et al. [2], Hummel [3], clearly show the secondary separation phenomenon, and in particular that the full pressure recovery beyond separation, of the inviscid model, is not achieved. Nutter [4] has presented an inviscid model of the secondary separation in which it is represented by a spiral vortex sheet that leaves the wing surface smoothly. In this inviscid model which, like the original model of Smith, is assumed to be conical the inviscid secondary separation line may be fixed arbitrarily on the wing surface. Nutter combines this with a classical laminar boundary-layer calculation. This is used to fix the position of flow separation by varying the position of the inviscid separation line until the boundary layer, developing in the given inviscid flow field, separates at the line of inviscid flow separation. The model itself is thus self-consistent. There is some experimental evidence, in the water-tunnel experiments of Thompson [5], which is in favour of this inviscid flow model. However, the pressure distributions which result from it are unlike any that have been observed in practice. A different approach has been adopted by Woodson and DeJarnette [6]. With the primary vortex configuration fixed they first determine the separation line from a classical boundary-layer calculation. Their viscous calculation then continues beyond separation using an inverse interactive method, with the no-slip condition replaced by conditions on the surface shear stress, both components of which are fixed at

the values at separation. The results obtained are more realistic than those of the inviscid model.

In the present paper we address the secondary separation problem using a viscous-inviscid interactive method which allows for modifications to the vortex-sheet configuration that models the primary separation. We assume throughout a laminar, incompressible flow situation. Our starting point is the inviscid, conical flow solution for primary separation which is based on the inviscid model of Smith [1]. With the pressure field and surface velocities given from this configuration, we solve the interactive boundary-layer equations over the wing surface and along the leading-edge vortex sheet. Although the interactive equations are multi-structured we treat them in the manner set out by Veldman [7] for two-dimensional flows. Thus the main viscous layer, and much thinner sub-layer, are accommodated within a layer which has the classical boundary-layer thickness. As has been shown by Riley [8] the interaction at very high Reynolds number, in the situation under consideration, is largely two-dimensional, and this is reflected in the form that the interaction law takes. The interaction modifies the transverse component of the slip velocity at the surface, that is the component perpendicular to the separation line. The concomitant modification we make to the radial component is based upon the conical flow assumption for the outer inviscid flow. From the viscous calculation we find the viscous displacement velocity over the wing surface and along the sheet. For the outer inviscid flow this displacement effect may be represented as a source distribution along the wing and the sheet. With this source distribution in place the outer inviscid flow is re-calculated to give new positions and strengths for the leading-edge vortex configuration. We now have a new inviscid flow-field with which to carry out the interactive calculation. This process is repeated until a converged solution is achieved.

The results we have obtained in the manner described above show qualitative agreement with the measured pressure distributions over the wing. Thus the suction rises to a peak value beneath the vortex core and after only a small pressure recovery, to the point where secondary separation takes place, there is a pressure plateau up to the leading edge. Over the Reynolds number range for which we have obtained solutions our pressure distributions display a conical character which is not a feature of the experimentally obtained results. For example, the experimental pressure measurements of Hummel [3] cannot be said to exhibit any conical features. Pressure levels increase monotonically from the apex to the trailing edge. Our predicted pressures are higher than the experimental values over the forward part of the wing, and lower than those over the rear portion. By contrast, geometric features of the real flows do exhibit conical flow features, and our estimates of the positions of the secondary separation line and the vortex cores show good quantitative agreement with experiment. We may conclude that our model of the secondary separation phenomenon is a significant improvement upon earlier models, and displays the main flow features that we attribute to secondary separation. However, it seems clear that to predict accurately the flow features when secondary separation is present, a three-dimensional model of the flow must be introduced. Such a model would incorporate many of the new features that we have introduced into the present model.

Our mathematical treatment of the problem is developed in Section 2, where we treat the inviscid flow model, and the viscous-inviscid interaction, separately and outline our overall solution strategy. Section 3 is devoted to the solution procedure whilst Section 4 contains a detailed discussion of the results we have obtained.

2. Mathematical treatment

2.1. The inviscid flow model

With reference to Fig. 1 we consider, in the slender body and conical flow approximations, the flow past a thin delta wing. With origin O at the wing apex the x'-axis forms the centre-line of the wing, the y'-axis is measured to starboard and the z'-axis is perpendicular to the wing. The undisturbed stream of speed U makes a small angle α with the x'-axis; γ is the semi-apex angle of the wing.

Outside the viscous layers, namely the boundary layer and free shear layers which form on the wing and at the source-vortex sheets respectively, we may treat the flow as an inviscid, irrotational flow. In this inviscid region we represent the velocity $\mathbf{V}'$ of the fluid in terms of the free stream U and a disturbance potential Φ' as

$$\mathbf{V}' = \nabla(Ux' + \Phi') , \tag{2.1}$$

where, within our slender treatment, Φ' satisfies the two-dimensional form of Laplace's equation

$$\Phi'_{y'y'} + \Phi'_{z'z'} = 0 , \tag{2.2}$$

and a subscript is to denote differentiation.

It is convenient to introduce dimensionless variables such that

$$x = Kx'/s , \qquad y = y'/s , \qquad z = z'/s , \qquad \Phi = \Phi'/KUs , \tag{2.3}$$

where $K = \tan\gamma$ and $s = Kx'$ is the semi-span of the wing. The potential Φ is the real part of a complex potential $W(Z)$ where $Z = y + iz$. Our problem now is to construct the complex potential W which satisfies all of the appropriate boundary conditions.

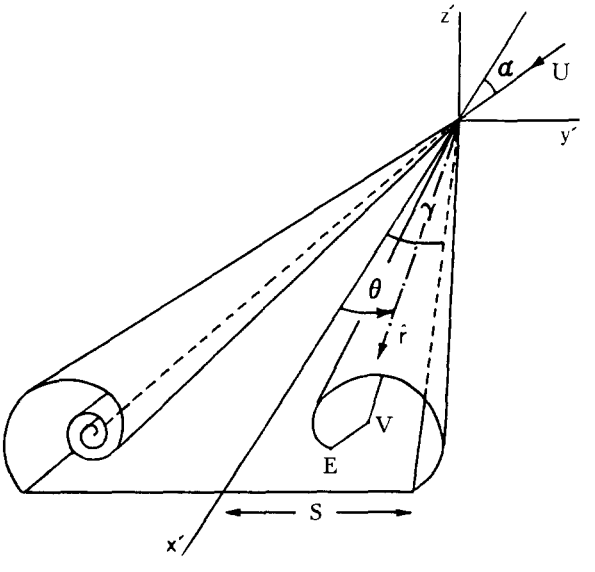

Fig. 1. The wing, vortex sheets and co-ordinate system.

Conditions at infinity, and on the wing surface, require

$$W + iaZ \to 0 \quad \text{as} \quad Z \to \infty , \tag{2.4}$$

and

$$\mathcal{I}m\left(\frac{dW}{dZ}\right) = -v_N \quad \text{at} \quad |y| \leq 1 , \quad z = 0 , \tag{2.5}$$

respectively, where $a = \alpha/K$ is the incidence parameter, and v_N is due to the viscous displacement effect.

The remaining conditions to be satisfied include conditions on the source-vortex sheet. As we have already indicated in Section 1 we represent the displacement effect of the viscous layers by source distributions not only on the wing but also on the sheets. In particular, such a distribution on the sheet has the effect of introducing a normal velocity v_N directed from the sheet into the flow on the inside of the sheet. If we take the outer surface of the sheet as a stream surface then, following Smith [1], we have on the outer surface,

$$\Phi_n = -r \sin \phi , \tag{2.6a}$$

where subscript n denotes the derivative in the direction of the unit inward normal to the trace of the sheet, and ϕ is the angle between the tangent and radius vector as shown in Fig. 2a. Since the normal velocity at the sheet is discontinuous, by an amount v_N, the corresponding condition on the inner surface of the sheet is

$$\Phi_n = -r \sin \phi + v_N . \tag{2.6b}$$

The remaining condition on the sheet is that the pressure jump across it $\Delta C_p = 0$. Here Δ represents the difference operator, inside minus outside, at the sheet and C_p is the pressure coefficient. The pressure coefficient is given by

$$C_p/K^2 = -2\Phi_x - (\Phi_y^2 + \Phi_z^2) + a^2 . \tag{2.7}$$

If we apply the operator Δ to equation (2.7), with $\Delta C_p = 0$, and use the fact that the sheet is conical, the pressure condition may then be written as

$$\Delta\Phi = \Delta\Phi_\sigma (r \cos \phi - \Phi_{\sigma_m}) - \tfrac{1}{2} v_N^2 , \tag{2.8}$$

where σ is arc length along the cross section of the sheet as in Fig. 2, and the suffix m denotes the mean value across the sheet. Finally, at the leading edge where the primary separation takes place, we impose the Kutta condition that the velocity is finite, that is

$$\frac{dW}{dZ} \text{ is finite at } y = \pm 1 , \quad z = 0 . \tag{2.9}$$

Following Smith [1] we do not attempt to satisfy (2.6a) and (2.8) at all points of the sheet, which is infinite in extent. Instead, we represent the source-vortex sheet by a finite part springing from the leading edge and an isolated line vortex, as shown on the starboard

half-wing in Fig. 1. The inner part of the sheet, beyond E, is concentrated into the line vortex at V. Across the cut, which is left behind, the velocity potential jumps by an amount equal to the circulation about the line vortex. Equation (2.8) cannot be satisfied at the cut and we replace it by the condition that the total force on the vortex and cut be zero. This condition of zero total force may be written, see Smith [1], as

$$\lim_{Z\to Z_V}\left(\frac{\mathrm{d}W}{\mathrm{d}Z}-\frac{\Gamma}{2\pi\mathrm{i}}\frac{1}{Z-Z_V}\right)=2\bar{Z}_V-\bar{Z}_E\,, \tag{2.10}$$

where Γ is the circulation of the starboard isolated vortex, Z_V and Z_E represent the positions of the isolated vortex and end of the cut respectively, and an overbar denotes the complex conjugate.

To construct the complex potential it proves convenient to introduce the conformal transformation

$$Z^{*2}=Z^2-1\,, \tag{2.11}$$

which maps the slit $|y|\leqslant 1$, $z=0$, that represents the cross-section of the wing in the Z-plane, to the slit $y^*=0$, $|z^*|\leqslant 1$ in the transformed plane, where $Z^*=y^*+\mathrm{i}z^*$. From symmetry considerations we see that in the Z^*-plane the wing condition (2.5) is automatically satisfied. We may then write the complex velocity in the transformed plane as

$$\begin{aligned}\frac{\mathrm{d}W}{\mathrm{d}Z^*}=&-\mathrm{i}a+\frac{\Gamma}{2\pi\mathrm{i}}\left(\frac{1}{Z^*-Z_V^*}-\frac{1}{Z^*+\bar{Z}_V^*}\right)\\&+\frac{1}{2\pi\mathrm{i}}\int_0^{\sigma^*_{\max}}g^*(\sigma^*)\left(\frac{1}{Z^*-Z^*(\sigma^*)}-\frac{1}{Z^*+\bar{Z}^*(\sigma^*)}\right)\mathrm{d}\sigma^*\\&+\frac{1}{\pi\mathrm{i}}\int_0^{i}\frac{v_N}{Z^*-t^*}\left|\frac{\mathrm{d}t}{\mathrm{d}t^*}\right|\mathrm{d}t^*\\&+\frac{1}{2\pi}\int_0^{\sigma^*_{\max}}v_N\left|\frac{\mathrm{d}Z}{\mathrm{d}Z^*}\right|\left(\frac{1}{Z^*-Z^*(\sigma^*)}+\frac{1}{Z^*+\bar{Z}^*(\sigma^*)}\right)\mathrm{d}\sigma^*\,.\end{aligned} \tag{2.12}$$

In (2.12) the first term represents the free stream whilst the second and third terms are contributions from the isolated vortices and the distributed vorticity, strength g^*, along the finite parts of the source-vortex sheets respectively. The remaining terms are a consequence of the distributed sources on the upper surface of the wing, and along the source-vortex sheets, due to the viscous displacement effect of the boundary layer and the free shear layers. Note that on each sheet the source strength vanishes before the end of the finite part of it at $\sigma^*_{\max}$. The condition (2.4) at infinity is satisfied automatically by (2.12). The remaining conditions, namely (2.6b), (2.8), (2.9) which is represented by the condition that $\mathrm{d}W/\mathrm{d}Z^*=0$ at $Z^*=0$ in the Z^*-plane, and (2.10) serve to determine the unknowns which are the strength Γ and position Z_V of the isolated vortices and the strength $g^*(\sigma^*)=-\mathrm{d}\Delta\Phi/\mathrm{d}\sigma^*$ and position of the finite parts of the source-vortex sheets. A discussion of the numerical procedures which implement the above conditions is deferred to Section 3.

2.2. The viscous-inviscid interaction

Central to our study of the thin viscous layers on the wing and the vortex sheet are the

classical laminar flow boundary-layer equations. In establishing these it proves convenient to employ the reduction of them used by Brown [9] for conical flow. Consider first the boundary layer on the upper surface of the wing. We work with cylindrical polar co-ordinates $(\hat{r}', \theta, z')$ with origin at the apex of the wing as in Fig. 1, and the corresponding velocity components (u', v', w'). The free-stream speed U is used to make velocities dimensionless, and in the spirit of boundary-layer theory we introduce the scaled variables

$$\xi = \frac{z'}{l}\left(\frac{l}{\hat{r}'}\right)^{1/2} \mathrm{Re}^{1/2}, \qquad \bar{w} = \frac{w'}{U}\left(\frac{\hat{r}'}{l}\right)^{1/2} \mathrm{Re}^{1/2}, \tag{2.13}$$

where $\mathrm{Re} = Ul/\nu$ is the Reynolds number, ν is the kinematic viscosity of the fluid and l is an arbitrary length. The further simplification, in which we write

$$\bar{w} = w + \tfrac{1}{2}\zeta u, \tag{2.14}$$

leads us, see [9], to the boundary-layer equations

$$\left.\begin{aligned} v\frac{\partial u}{\partial \theta} + w\frac{\partial u}{\partial \zeta} - v^2 - \frac{\partial^2 u}{\partial \zeta^2} &= v_e\left(\frac{\mathrm{d}u_e}{\mathrm{d}\theta} - v_e\right), \\ v\frac{\partial v}{\partial \theta} + w\frac{\partial v}{\partial \zeta} + uv - \frac{\partial^2 v}{\partial \zeta^2} &= v_e\left(\frac{\mathrm{d}v_e}{\mathrm{d}\theta} + u_e\right), \\ \tfrac{3}{2}u + \frac{\partial v}{\partial \theta} + \frac{\partial w}{\partial \zeta} &= 0. \end{aligned}\right\} \tag{2.15a,b,c}$$

In equations (2.15) the external velocity components (u_e, v_e) on the wing surface may be expressed in terms of the potential Φ of Section 2.1 as

$$\left.\begin{aligned} u_e = u_{ep} &= (1 - \tfrac{1}{2}\alpha^2 + K^2\Phi_x)\cos\theta + K\Phi_y \sin\theta, \\ v_e = v_{ep} &= K\Phi_y \cos\theta - (1 - \tfrac{1}{2}\alpha^2 + K^2\Phi_x)\sin\theta. \end{aligned}\right\} \tag{2.16a,b}$$

For the viscous shear layers on the source-vortex sheets we ignore curvature effects in the boundary-layer equations so that equations (2.15) are still appropriate, as if the sheets had been 'unrolled' onto the plane $z = 0$. To find the quantities (u_e, v_e) analogous to (2.16) on the sheet we proceed as follows. If $\mathbf{r}_s$ is the position vector of a point on the conical vortex sheet we have immediately, with reference to the rectangular axes of Section 2.1, that

$$u_e = u_{ep} = \frac{\mathbf{V}\cdot\mathbf{r}_s}{|\mathbf{r}_s|} = \frac{1 - \tfrac{1}{2}\alpha^2 + K^2\Phi_x + K^2 y\Phi_y + K^2 z\Phi_z}{\{1 + K^2(y^2 + z^2)\}^{1/2}}. \tag{2.17a}$$

For the corresponding component of velocity v_e we then have

$$v_e = \left|\mathbf{V} - \frac{u_e \mathbf{r}_s}{|\mathbf{r}_s|}\right| + O(v_N^2)$$

from which we deduce, using (2.17a), that

$$v_e = v_{ep} = (A^2 + B^2 + C^2)^{1/2} + O(v_N^2), \tag{2.17b}$$

where

$$A = 1 - \tfrac{1}{2}\alpha^2 + K^2\Phi_x - u_e/\{1 + K^2(y^2 + z^2)\}^{1/2},$$

$$B = K\Phi_y - u_e Ky/\{1 + K^2(y^2 + z^2)\}^{1/2},$$

$$C = K\Phi_z - u_e Kz/\{1 + K^2(y^2 + z^2)\}^{1/2}.$$

As we have remarked already in Section 1, and discuss further below, all our viscous calculations take place on the upper surface of the wing, where the secondary separation occurs. As a consequence all quantities in (2.16) are evaluated on the upper surface of the wing, and all quantities in (2.17a), (2.17b) on the inner side of the sheet. The boundary conditions for (2.15) require that the solution match with the external flow (u_e, v_e), and that the solution is given at the line of attachment $\theta = \theta_a$. In addition we have the no-slip condition at $\zeta = 0$ on the wing, whilst on the sheet we have adopted the conditions that $w = u\zeta = v\zeta = 0$ at $\zeta = 0$. This latter assumption that the sheet is a stress-free boundary is an approximation. The complete problem requires the solution on the lower wing surface and matching of the solution with the flow on the outer side of the sheet. However, the dominant feature of the flow is the secondary separation on the upper surface of the wing, and as we demonstrate later the boundary conditions adopted for (2.15) at $\zeta = 0$ on the sheet have a negligible effect on the overall flow properties.

Note that with the introduction of the variables (2.14) all flow quantities are independent of $\hat{r}$ in the conical flow approximation. This means that the right-hand side of (2.15a) should be set to zero representing, as it does, the surface pressure gradient $-\partial p/\partial \hat{r}$. However, it is retained for the moment, for reasons which will become clear in Section 2.3 below.

It is well known that if in a two-dimensional laminar boundary-layer calculation a region of adverse pressure gradient is encountered which leads to flow separation, then the solution develops a singularity at the point of separation defined as the point of vanishing skin friction. In the problem under discussion here adverse pressure gradients on the upper surface of the wing are known to result in flow separation. Nutter [4] has demonstrated that the solution of (2.15) with (2.16) does indeed result in singular behaviour at separation. Catherall and Mangler [10], by working in an inverse mode in which the displacement thickness is prescribed, demonstrate that the singularity is removed if the pressure is allowed to adjust to the local flow conditions. Subsequent work by Sychev [11] and Smith [12] has revealed that the interactive coupling between the boundary layer and the potential flow region is crucial in a description of the regular behaviour of the flow at separation. The asymptotic theory for large Reynolds number involves a triple-deck structure centered upon the point of separation. Veldman [7] has argued that there appears to be little to gain, in a practical situation, by attempting to form a composite solution from the expansions in the different domains of the asymptotic solution. Rather more profitable, he suggests, is an approach in which a composite equation is used which reflects the main features of the asymptotic solution. It is in such a spirit that we proceed in the present situation.

The two-dimensional asymptotic theory [11, 12] has been adapted by Riley [8] for slender conical flows of the type under consideration here. Our aim is to ensure that the dominant features of that theory are retained in our present treatment. The main deck of the triple-deck theory has thickness $O(l\,\mathrm{Re}^{-1/2})$, a scaling on which our equations (2.15) are based. The lower deck, of thickness $O(l\,\mathrm{Re}^{-5/8})$ is embedded within this. Thus if at a large, but finite, Reynolds number sufficient numerical resolution is available (2.15) will encompass

both the lower and main decks. In the region outside the main deck the perturbation to the inviscid potential flow is 'driven' by the viscous displacement velocity w_d. The asymptotic theory [8] shows that since the changes which take place normal to the separation line in this slender conical flow are very rapid, compared with those parallel to it, the flow structure exhibits many of the features of a two-dimensional flow. If therefore we write $\xi = \hat{r}'\theta/l$, $\eta = z'/l$ the equation satisfied by the perturbation potential $\tilde{\Phi} = \tilde{\Phi}'/Ul$, due to the displacement velocity, is simply

$$\tilde{\Phi}_{\xi\xi} + \tilde{\Phi}_{\eta\eta} = 0 . \tag{2.18}$$

The solution of (2.18) is to vanish as $\xi^2 + \eta^2 \to \infty$, and on $\eta = 0$, $\tilde{\Phi}_\eta = (l/\hat{r}')^{1/2}\,\mathrm{Re}^{-1/2} w_d$. The solution for $\tilde{\Phi}$ yields a perturbation to the slip velocity v_e such that we have

$$v_e = v_{ep} + \frac{\mathrm{Re}^{-1/2}}{\pi}\left(\frac{l}{\hat{r}'}\right)^{1/2} \int \frac{w_d}{\xi - \xi'}\,\mathrm{d}\xi' , \tag{2.19}$$

where v_{ep} is as defined in (2.16b), (2.18). If we now let $\hat{r}' = l$ then (2.19) becomes

$$v_e = v_{ep} + \frac{\mathrm{Re}_r^{-1/2}}{\pi} \int \frac{w_d}{\theta - \xi'}\,\mathrm{d}\xi' , \tag{2.20}$$

where $\mathrm{Re}_r = U\hat{r}'/\nu$, so that we now have a representation of the flow which is locally conical. In (2.19), (2.20) the integration extends over the interaction region which encompasses both the separation and reattachment points. The latter may, of course, be on the source-vortex sheet itself. To complete our formulation of the problem we need an expression for the viscous displacement velocity. If we again reflect the two-dimensional nature of the flow in the interaction region, as suggested by the asymptotic theory of [8], then we write

$$w_d = \frac{\partial}{\partial\theta}\int_0^\infty (v_e - v)\,\mathrm{d}\zeta . \tag{2.21}$$

In broad outline the formulation of our problem is now complete. But before we present the numerical scheme which we have implemented for its solution, we now outline our strategy for the solution.

2.3. Solution strategy

The solution strategy we have adopted for the highly non-linear problem outlined in Sections 2.1, 2.2 involves several iterative processes. These, together with the numerical schemes we have used to implement them, are outlined in some detail in Section 3. Here we give a brief indication of our overall strategy.

Our first task is to obtain a solution of the inviscid problem outlined in Section 2.1. The initial solution of this problem is with $v_N \equiv 0$, and corresponds to the original solutions of Smith [1]. With this inviscid solution in place, giving the 'slip' velocity components u_{ep}, v_{ep}, we are then in a position to study the viscous boundary layers and shear layers. In his work, Nutter [4] used the classical boundary-layer equations for the boundary layer on the wing surface. His calculations terminated in a singularity at the line of secondary separation. Our approach is the viscous-inviscid interactive approach outlined in Section 2.2. Thus, in order

to avoid the singular behaviour, we allow the pressure to adjust itself as the step-by-step integration of the equations (2.15) is carried out. This, in practice, leads to a continuous adjustment of the external velocity component v_e, at a fixed Re_r, as in equation (2.20). As we advance the solution on the upper surface beyond the secondary separation line on the wing, a region of reversed flow is encountered. To continue the forward integration into this region it has been found necessary to employ the FLARE approximation in (2.15). Beyond the leading edge of the wing the boundary layers from the upper and lower wing surfaces merge. However, our treatment of the problem does not explicitly include a calculation on the lower wing surface. For the solutions we present in Section 4 below, we have replaced the condition that the upper and lower boundary layers merge smoothly, with the condition on the upper boundary layer that at $\zeta = 0$, $u_\zeta = v_\zeta = 0$. Tests we have carried out indicate that the solution is not sensitive to this boundary condition. Between separation and the reattachment which takes place on the sheet, there is a region of reversed flow. As a consequence the viscous solution cannot be completed in one sweep from the line of attachment to the end of point of the calculation, which is taken as a point where $|v_e - v|$ is sufficiently small across the shear layer. Further sweeps are necessary with v_{ep} in (2.20) fixed. At the commencement of each sweep u_e is changed. Initially it takes the value u_{ep} in (2.16a), but is updated at the commencement of each sweep from the equation $\mathrm{d}u_e/\mathrm{d}\theta = v_e$ in order to maintain local conicality.

When the above iterative procedure is deemed to have converged we may up-date the outer inviscid solution. The changes to this are brought about by the displacement effect of the wing boundary layers, and the shear layers. With w_d as in (2.21) we have $v_N = w_d/K\,\mathrm{Re}_r^{1/2}$ to represent the displacement effect in the inviscid solution. The inviscid solution is now recalculated to provide new values of the slip velocity (u_{ep}, v_{ep}). The viscous solution is then completed as before with one slight modification. Since the displacement effect is now included in the inviscid solution, as well as in (2.20), we modify (2.20) such that

$$v_e = v_{ep} + \frac{\mathrm{Re}_r^{-1/2}}{\pi} \int \frac{w_d - w_{dp}}{\theta - \xi'}\,\mathrm{d}\xi' \,. \tag{2.22}$$

Here w_{dp} is the displacement velocity which has been obtained in the previous viscous calculation, and the displacement effect is not now duplicated.

The overall iterative procedure outlined above is continued until convergence according to some pre-set criteria has been obtained. In the converged solution we have $w_d = w_{dp}$, the right-hand side of (2.15a) is zero, and the velocities v_N, w_d, which represent the displacement effect in the inviscid and viscous solutions respectively, are self-consistent. The numerical schemes which enable this are outlined in the next section.

3. Solution procedure

The overall numerical treatment is in two parts, and deals separately with the inviscid flow model of Section 2.1 and the viscous-inviscid interaction of Section 2.2.

3.1. The inviscid flow model

In the inviscid flow model the unknowns are the position Z_V^* and strength Γ of the isolated vortex, together with the position $Z^*(\sigma^*)$ and the strength $g^*(\sigma^*)$ of the vortex sheet. These

are to be determined from the conditions on the sheet, namely (2.6a,b), (2.8), on the isolated vortex and cut (2.10), and the Kutta condition (2.9). We note that in this part of the solution procedure the viscous displacement velocity is treated as a known quantity, given as it is from the interactive part of the calculation. For the initial inviscid flow solution, which serves as the base for our whole solution procedure, we have $v_N \equiv 0$. Such solutions correspond to the original inviscid solutions of Smith [1].

Our solution procedure follows very closely that of Barsby [13], which is a development of that originally introduced by Smith [1]. Thus we introduce the intrinsic co-ordinates (σ^*, ψ^*) of Fig. 2b in the transformed plane so that

$$Z^*(\sigma^*) = \int_0^{\sigma^*} e^{i\psi^*(s)}\, ds\,, \tag{3.1}$$

where $Z^*(0) = 0$. In order to perform the numerical integrations around the sheet we divide it into $2n$ equal steps of length h of arc length σ^*, and so define $2n+1$ pivotal points in terms of the angle ψ^* at these points. The length of the finite part of the sheet is then determined by the values of h and n. The first of these pivotal points coincides with the leading edge of the wing where it may be shown that $\psi^*(0) = 0$. It can also be shown that at the leading edge $g^*(0) = 0$. Midway, in terms of arc length σ^*, between each pivotal point we introduce an intermediate point (see Fig. 2b). The values of the quantities under consideration at the intermediate points are denoted by a tilde, and it is at these points that we determine the $4n$ unknowns $\tilde{\psi}_i^*$, $\tilde{g}_i^*$, $i = 1, 2, \ldots, 2n$. These unknowns together with Z_V^* and Γ give us a total of $4n+3$ unknown quantities which are determined by the force and Kutta conditions, (2.10), (2.9) respectively, together with the sheet conditions (2.6a,b), (2.8). These latter are combined to give, on the source-vortex sheet (see Appendix)

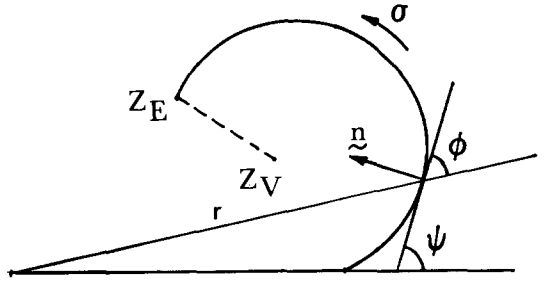

Fig. 2a. Axes, and co-ordinates in the cross-flow plane.

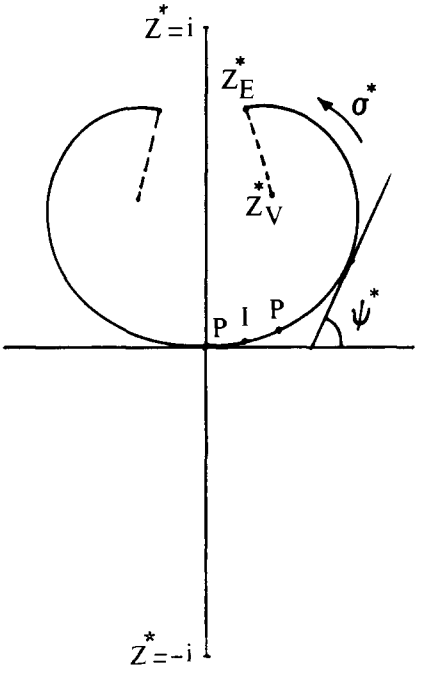

Fig. 2b. Configuration in the transformed plane. *P* pivotal, *I* intermediate point.

$$-g^*(\sigma^*)\,\mathrm{e}^{\mathrm{i}\psi^*}\left|\frac{\mathrm{d}Z^*}{\mathrm{d}Z}\right|^2\left(\bar{Z}\,\frac{\mathrm{d}Z}{\mathrm{d}Z^*}-\frac{\mathrm{d}W}{\mathrm{d}Z^*}\right)+\frac{\mathrm{i}}{2}\,g^*(\sigma^*)\left|\frac{\mathrm{d}Z^*}{\mathrm{d}Z}\right|v_N-\tfrac{1}{2}v_N^2=\Gamma+\int_{\sigma^*}^{\sigma^*_{\max}}g^*(s)\,\mathrm{d}s\,. \tag{3.2}$$

These conditions give a total of $4n+3$ nonlinear algebraic equations to solve for the unknown quantities. With the values of $\tilde{\psi}_i^*$, $\tilde{g}_i^*$ determined at the intermediate points the values of ψ^*, g^* at the pivotal points are then obtained by 4-point Lagrangian interpolation.

All the conditions to be satisfied involve an evaluation of $\mathrm{d}W/\mathrm{d}Z^*$ at the appropriate intermediate point. The integrals in the third and fifth terms of (2.12) are evaluated by using Simpson's rule. For points on the sheet the integrals are interpreted as Cauchy Principal Values, and in order to employ Simpson's rule the singularity is removed in the following manner,

$$\int\frac{p(t)\,\mathrm{d}t}{t-t_0}=\int\frac{p(t)-p(t_0)}{t-t_0}\,\mathrm{d}t+p(t_0)\int\frac{\mathrm{d}t}{t-t_0}\,. \tag{3.3}$$

The first integral in (3.3) may now be evaluated numerically making use of l'Hôpital's rule, and the second in closed form. The fourth term in (2.12), which represents the effect of the wing source distribution, due to the viscous displacement of the boundary layer, is evaluated by the Gaussian 5-point rule.

We now have, from equations (2.9), (2.10) and (3.2) a total of $4n+3$ non-linear equations for the $4n+3$ unknown quantities. These are Z_V^*, Γ together with $\tilde{\psi}_i^*$, $\tilde{g}_i^*$ at the $2n$ intermediate points on the sheet. To solve these equations we write them in the form

$$f_i(\mathbf{x})=0\,,\quad i=1,2,\ldots,4n+3\,, \tag{3.4}$$

where $\mathbf{x}$ is the solution vector for the $4n+3$ unknowns. From a reasonable initial guess of the solution we use the Newton iterative procedure to complete it, thus

$$\mathbf{x}^{k+1}=\mathbf{x}^k-(\mathbf{J}^k)^{-1}\mathbf{f}^k\,, \tag{3.5}$$

where $\mathbf{J}^k=(\partial f_i/\partial x_j)$ is the Jacobian matrix, and $\mathbf{x}^k$ denotes the k^{th} iterate in the solution procedure. The iterative procedure is deemed to have converged when the sum of the absolute values of the residual functions f_i is less than 10^{-6}.

With Z_V^*, Γ together with ψ^*, g^* at all points on the sheet now known we can readily evaluate physical quantities of interest such as the total circulation

$$\Gamma+\int_0^{\sigma^*}g^*(\sigma^*)\,\mathrm{d}\sigma^*\,, \tag{3.6}$$

the pressure distribution given by (2.7), and the external velocity components on the wing surface and on the source vortex sheet defined in equations (2.16a,b), (2.17) and (2.18). These velocity components serve as edge conditions for the boundary layer, and their detailed derivation is given in the Appendix.

3.2. The viscous-inviscid interaction

With an updated solution of the inviscid-flow problem determined for a given incidence parameter a, the corresponding slip velocities u_{ep}, v_{ep} may be calculated and the interactive

boundary-layer equations solved for a given Reynolds number Re_r. Note that for the first boundary-layer solution, using the initial inviscid solution, we have $w_{dp} \equiv 0$.

The numerical solution of the boundary-layer equations (2.15a,b,c) is carried out using the Keller box method [14] in a form which allows us to exploit Veldman's quasi-simultaneous interactive procedure. With Keller's box method equations (2.15a,b,c) are written as a first-order system, thus

$$\left.\begin{aligned}
&\frac{\partial u}{\partial \zeta} = g\,, \\
&\frac{\partial v}{\partial \zeta} = p\,, \\
&\frac{\partial g}{\partial \zeta} - wg + v^2 - v\,\frac{\partial u}{\partial \theta} - v_e\left(v_e - \frac{\mathrm{d}u_e}{\mathrm{d}\theta}\right) = 0\,, \\
&\frac{\partial p}{\partial \zeta} - wp - uv - v\,\frac{\partial v}{\partial \theta} + v_e\left(u_e + \frac{\mathrm{d}v_e}{\mathrm{d}\theta}\right) = 0\,, \\
&\tfrac{3}{2}u + \frac{\partial v}{\partial \theta} + \frac{\partial w}{\partial \zeta} = 0\,.
\end{aligned}\right\} \qquad (3.7a,b,c,d,e)$$

The boundary conditions for equations (3.7) for flow over the wing are

$$\left.\begin{aligned}
&u = v = w = 0 \quad \text{at} \quad \zeta = 0\,, \\
&u \to u_e(\theta)\,, \quad v \to v_e(\theta) \quad \text{as} \quad \zeta \to \infty\,,
\end{aligned}\right\} \qquad (3.8a,b)$$

together with initial conditions at the line of attachment $\theta = \theta_a$ at which the numerical scheme for the boundary-layer equations is initiated. The attachment-line solution is discussed at the end of this section. As we have already indicated we adopt a stress-free boundary condition on the source-vortex sheet so that we have there

$$\left.\begin{aligned}
&\frac{\partial u}{\partial \zeta} = \frac{\partial v}{\partial \zeta} = w = 0 \quad \text{at} \quad \zeta = 0\,, \\
&u \to u_e(\theta)\,, \quad v \to v_e(\theta) \quad \text{as} \quad \zeta \to \infty\,.
\end{aligned}\right\} \qquad (3.9a,b)$$

The interactive law (2.22) is used in the form

$$v_e(\theta) = v_{ep}(\theta) + \frac{\mathrm{Re}_r^{-1/2}}{\pi} \int_{\theta_a}^{\theta_b} \frac{\dfrac{\mathrm{d}}{\mathrm{d}\xi}(f - f_p)}{\theta - \xi}\,\mathrm{d}\xi \qquad (3.10)$$

where the quantity f, with $\partial f/\partial\theta = w_d$ has been introduced for computational convenience. It has been assumed in (3.10) that the region of strong interaction is confined to the interval $\theta_a \leqslant \theta \leqslant \theta_b$.

Following Veldman [7] we discretise (3.10) and express it in the form

$$v_{ei} - 4cf_i = \Lambda_i\,, \qquad (3.11)$$

where v_{ei} and f_i are the unknown quantities at a streamwise location θ_i, and

$$c = \mathrm{Re}_r^{-1/2}/\pi\,\Delta\theta\,, \tag{3.12a}$$

$$\Lambda_i = v_{ep}(\theta_i) + c\Bigg[\sum_{\substack{j=1\\ j\neq i-1,i}}^{N} \{(f-f_p)_{j+1} - (f-f_p)_j\}\log\left|\frac{i-j}{i-j-1}\right| - 2\{(f-f_p)_{i+1} + (f-f_p)_{i-1}\} - 4f_{p_i}\Bigg]\,, \tag{3.12b}$$

for a uniform grid $\Delta\theta$ in the θ-direction.

In order to complete the system of equations we may express (2.21), using (2.15c), as

$$\frac{\partial f}{\partial\theta} = w|_{\zeta_\infty} + \tfrac{3}{2}\int_0^{\zeta_\infty} u\,\mathrm{d}\zeta + \frac{\mathrm{d}v_e}{\mathrm{d}\theta}\,\zeta_\infty\,, \tag{3.13}$$

where ζ_∞ is the computational edge of the boundary layer, representing the point at infinity.

The discretised form of (3.7) and (3.10), together with (3.8), (3.9) and (3.13), yield a system of nonlinear algebraic equations for the unknowns u, v, v_e, f and w. Newton's method is again employed to linearise these equations resulting in a matrix of coefficients which is of 5×5 block tridiagonal form with an additional column of 5×5 matrices. The equations are solved by the block-elimination method. Further details of the derivation of the finite-difference equations together with their linearisation and solution will be supplied on request.

The line of attachment on the wing surface is defined as the line along which $v_e(\theta) = 0$, and is identified from the inviscid solution. At the stagnation line we write $v = \theta F(\zeta)$, $v_e = a_0\theta$ where $a_0 = (\mathrm{d}v_e/\mathrm{d}\theta)_{\theta_a}$. The stagnation-line equations then follow as

$$\left.\begin{aligned} &u'' - wu' = 0\,,\\ &F'' - F^2 - wF' - uF + a_0\{u_e(\theta_a) + a_0\} = 0\,,\\ &w' + \tfrac{3}{2}u + F = 0\,, \end{aligned}\right\} \tag{3.14}$$

where a prime denotes differentiation with respect to ζ, together with

$$\begin{aligned} &u = F = w = 0 \quad \text{at} \quad \zeta = 0\,,\\ &u \to u_e(\theta_a)\,, \quad F \to a_0 \quad \text{as} \quad \zeta \to \infty\,. \end{aligned} \tag{3.15}$$

The stagnation-line equations are also solved by the box method.

Numerical solution of the boundary-layer equations commences with the attachment-line profiles. Initially the solution is advanced using the classical boundary-layer equations only. A switch to the interactive scheme, outlined above, is made when the region of strong interaction is encountered. In the regions of strong interaction, where the pressure gradient is initially adverse, flow separation and concomitant flow reversal is encountered. In order to continue the forward integration it has been found necessary to employ the FLARE approximation to the streamwise convective terms in the momentum equations (3.7c,d). Also, because of the elliptic character of our interactive equations, implied by the interactive law (3.10), it is necessary to make several sweeps along the boundary layer to obtain a converged solution. The solution is deemed to have converged when

$$\max_i |f^k(\theta_i) - f^{k-1}(\theta_i)| \leq 10^{-4},$$

where k denotes the iteration number. When the boundary-layer solution is complete we may return to the inviscid flow, Section 3.1, and continue with the global iterative scheme.

4. Results and discussion

As we have already indicated, the starting point for our solutions is the inviscid-flow model in which the primary separation is represented by a vortex sheet springing from the leading edge. Our calculations are carried out in the transformed plane defined by equation (2.11), and the method of solution is described in Section 3.1. We have chosen to work with nine pivotal points and eight intermediate points so that, in the notation of Section 3.1, $n = 4$. We determine the spacing, in terms of arc length σ^*, between the pivotal points from $h = |Z_V^*|/C$. With $n = 4$ we find that a value $C = 5.4$ gives a good representation of the vortex configuration as compared, for example, with the results of Smith [1]. We concentrate initially on the situation for which the incidence parameter $a = 1$. The slip velocities u_{ep}, v_{ep} on the upper surface of the wing and on the inner side of the vortex sheet are determined from equations (2.17). In Fig. 3 we show the component of velocity v_{ep}.

The next stage of the iterative calculation is to implement the interactive procedure of Section 2.2 where, in equation (2.22) v_{ep} is as shown in Fig. 3 and $w_{dp} \equiv 0$. We concentrate initially on the case for which the Reynolds number $\mathrm{Re}_r = 5 \times 10^4$. In all the cases considered we have adopted a wing of semi-apex angle $\gamma = 10°$ with 51 grid points on the wing surface corresponding to $\delta\theta = 0.2° \approx 3.491 \times 10^{-3}$ radians. The number of similarly spaced points on the vortex sheet varies with incidence parameter a. The calculation on the sheet extends to the point at which the viscous displacement velocity w_d is essentially zero. Thus, for $a = 1$, there are 32 such grid points on the sheet. The extent of the computational domain normal to the wing surface is dependent upon the Reynolds number, and increases as the Reynolds number increases. Typically $\zeta_\infty = O(10^2)$. We have used a variable mesh size which varies, typically, from $\delta\zeta = 0.025$ close to the boundary to $\delta\zeta = 0.5$ at the outer edge of the boundary layer. The viscous calculation is initiated at the line of attachment which for the case $a = 1$ is, as seen in Fig. 3, the wing centre-line. As we see from that figure the flow in

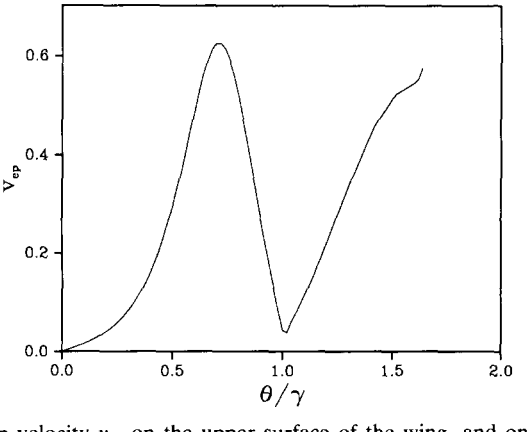

Fig. 3. Distribution of the slip velocity v_{ep} on the upper surface of the wing, and on the inner side of the vortex sheet, determined from the inviscid flow model for $a = 1$ when $w_d = 0$.

the θ-direction accelerates to a maximum, which is located beneath the isolated vortex, and then decelerates as the leading edge is approached. In this outboard region the pressure gradient is adverse and, unless the Reynolds number is sufficiently low, the flow will separate. When flow separation takes place it is in general, and certainly for Reynolds number $\mathrm{Re}_r = 5 \times 10^4$, necessary to use the FLARE approximation in which the streamwise convective terms in equations (3.7c,d) are neglected in the region of reversed flow. However we note that at lower values of Re_r, when there is a more modest region of reversed flow, it has been possible to incorporate the neglected terms as 'forcing' terms, evaluated from the previous sweep, in the equations. When successive sweeps lead to convergence, we then have a converged solution of the complete equations. Comparison between such a solution and the corresponding FLARE solution shows them to be almost identical giving us confidence in the FLARE approximation that has been expressed by others. Since we do not simultaneously calculate the boundary layer on the lower surface of the wing we comment again on the condition we have used on the sheet. For all the calculations described in this section we have assumed the sheet to be a stress-free surface. However, numerical experiments in which the condition is varied from no-slip to a negative shear stress give results which are virtually identical. The main feature which controls the overall flow properties is the separation and displacement effect on the wing surface. As we have already noted in Section 3.2, the elliptic character of our interactive equations, implied by (3.10), means that even when the FLARE approximation is employed several sweeps along the boundary layer, for a given v_{ep}, are necessary to obtain a converged solution. Typically 30 to 40 such sweeps are required. In Fig. 4 we show results of our interactive calculation which correspond to the velocity component v_{ep} of Fig. 3. Figure 4(a) shows the distribution of v_e as defined in equation (2.22). This inviscid slip velocity is already markedly different from that of the original inviscid solution. In Fig. 4(b) we show the viscous displacement velocity determined from this interactive calculation. This distribution of displacement velocity is quite typical of our calculations showing, as it does, outflow from the separated flow region over the wing, and entrainment into the viscous shear layer beyond the leading edge. It is the viscous displacement velocity which now provides the source distribution that features in the boundary condition (3.2) on the source-vortex sheet. A new inviscid solution is now

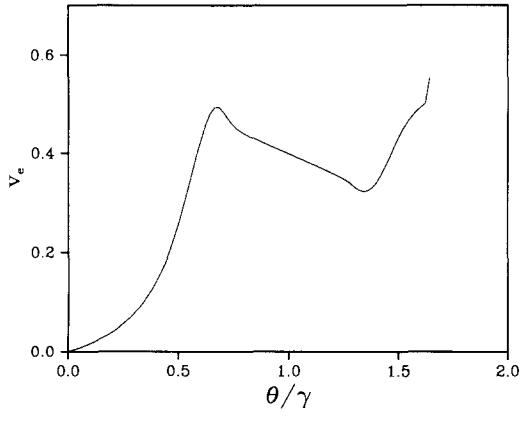

Fig. 4a. The distribution of v_e obtained from the first boundary layer interactive calculation; $a = 1$, $\mathrm{Re}_r = 5 \times 10^4$.

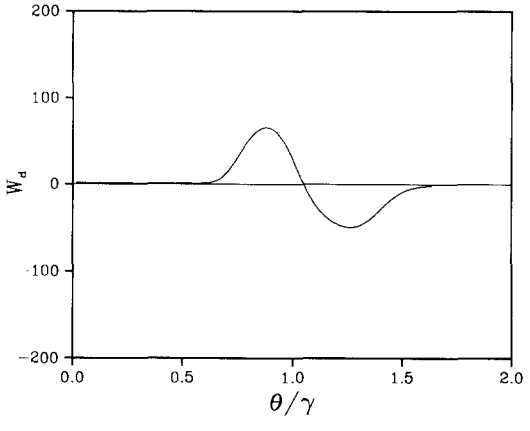

Fig. 4b. The viscous displacement velocity w_d determined from the first boundary layer interactive calculation; $a = 1$, $\mathrm{Re}_r = 5 \times 10^4$.

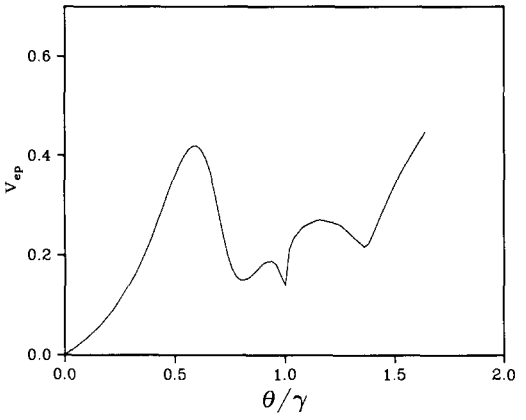

Fig. 5. Distribution of v_{ep} determined from the inviscid flow model with w_d as in Fig. 4b; $a = 1$, $\mathrm{Re}_r = 5 \times 10^4$.

obtained, incorporating the source distribution on the wing and sheet, as described in Section 3.1. From that solution we show, in Fig. 5, the newly obtained v_{ep}.

The procedure outlined above, which leads to the distributions of v_e, Fig. 4(a), and the updated v_{ep}, Fig. 5, from the viscous and inviscid calculations respectively, we term as one global iteration. This procedure is now repeated until the difference between these distributions is sufficiently small that the solution may be deemed to have converged. The convergence history of the procedure is illustrated in Figs 6 to 8 in which the results from alternate global iterations are presented. The solution which we accept as the converged result in this case of $a = 1$, $\mathrm{Re}_r = 5 \times 10^4$ is from the tenth global iteration. There are several features associated with these results which are worthy of comment. The first is that in the distributions of v_{ep} we have been unable to eliminate the small irregularity which appears beyond the leading edge, and in its immediate vicinity. The cause of this irregularity is not clear to us. A second point of interest is that from the fifth global iteration onward the distribution of v_e from the viscous part of the calculation is virtually unchanged. Indeed on the wing itself v_e and v_{ep} coincide after these five global iterations. It has been our practice after six or seven global iterations to introduce underrelaxation such that $v_{ep} = 0.5(v_e + v_{ep})$, which does of course leave v_{ep} unchanged on the wing. The reason that the rate of

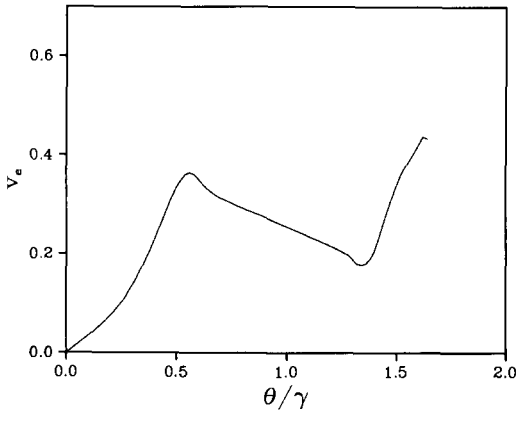

Fig. 6a. The slip velocity v_e obtained from the second boundary layer interactive calculation; $a = 1$, $\mathrm{Re}_r = 5 \times 10^4$.

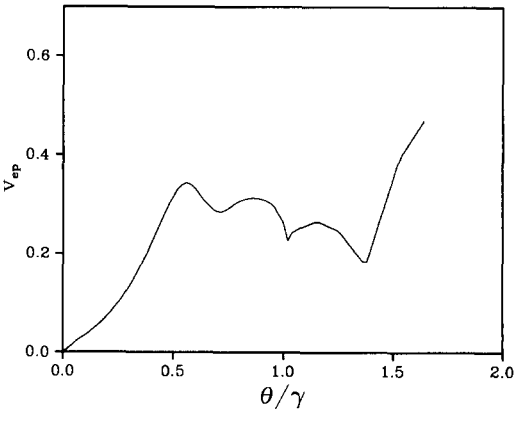

Fig. 6b. The distribution of v_{ep} from the second global iteration; $a = 1$, $\mathrm{Re}_r = 5 \times 10^4$.

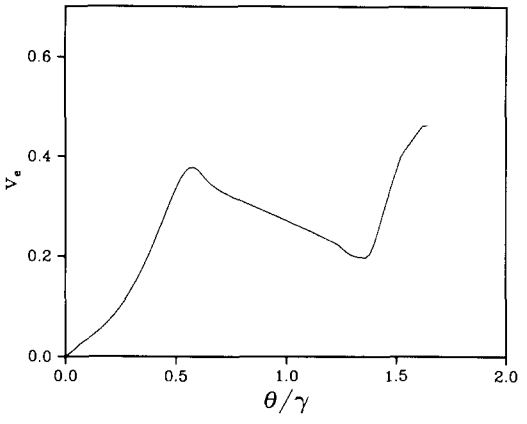

Fig. 7a. As Fig. 6a, sixth interactive calculation.

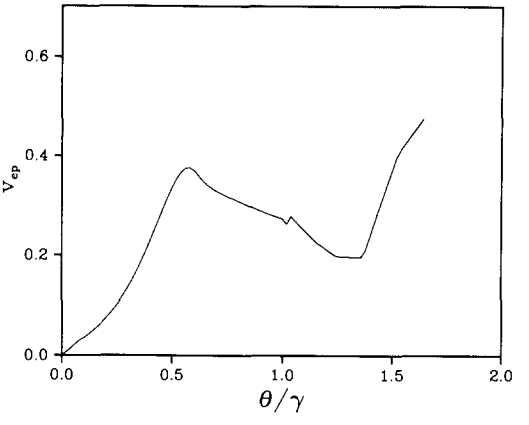

Fig. 7b. As Fig. 6b, sixth global iteration.

convergence of v_{ep} is lower than that of v_e is associated with the changes which take place in the source and vortex strengths on the source-vortex sheet during each global iteration. These are small enough not to affect the result of the viscous-inviscid interactive calculation, but not sufficiently small that changes in flow properties calculated from the inviscid solution, particularly in the neighbourhood of the sheet, may be ignored. The implication of this is that important features of the flow, for example the distribution of pressure over the surface of the wing, may be estimated before complete convergence has been achieved on the sheet itself. The results we present subsequently in this Section, unless otherwise stated, have been obtained on that basis.

As we have already remarked the source-vortex sheet configuration changes from that of the primary inviscid-flow model. In Fig. 9 we illustrate this point by making a comparison between the results from the initial inviscid solution and the results after one and ten global iterations. We see that when compared with Smith's [1] inviscid solution the isolated vortex core is moved both upward and inward. This is also true for other values of a and Re_r, and is in accord with experiment as we shall see later. In Fig. 10 we show the pressure distribution over the wing surface and sheet, calculated from our iterative procedure, where it is compared with the initial inviscid solution, namely the solution of Smith [1]. We see that the

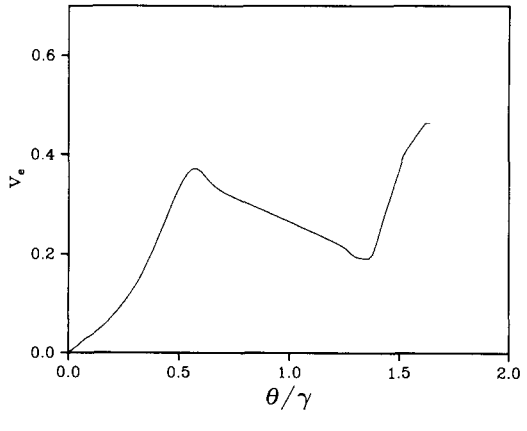

Fig. 8a. As Fig. 6a, tenth interactive calculation.

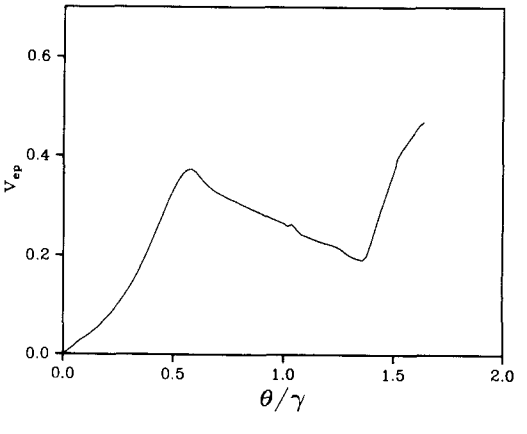

Fig. 8b. As Fig. 6b, tenth global iteration.

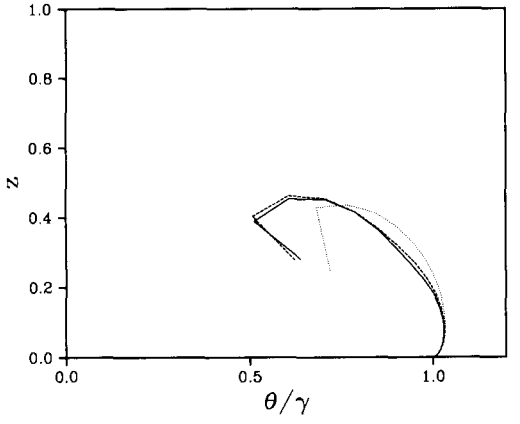

Fig. 9. Sheet configurations. (. . . . .) initial inviscid solution, (-----) inviscid solution after one global iteration, (——) and after ten global iterations; $a = 1$, $\mathrm{Re}_r = 5 \times 10^4$.

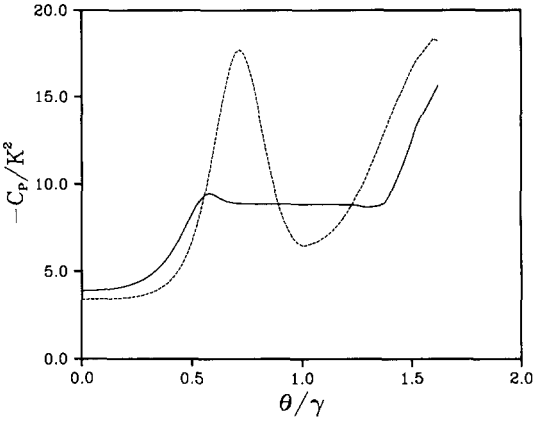

Fig. 10. Pressure distributions on the upper surface of the wing and sheet. (-----) initial inviscid solution, (——) converged interactive solution; $a = 1$, $\mathrm{Re}_r = 5 \times 10^4$.

suction peak is lower and, as may be expected when there is a region of separated flow, there is not a full pressure recovery beyond flow separation. This is qualitatively in accord with experimental results as we discuss later. For this particular case, flow separation takes place at $\theta/\gamma = 0.679$, which may be compared with the value $\theta/\gamma = 0.761$ obtained by Nutter [4], based on a boundary-layer calculation, and $\theta/\gamma = 0.607$ which Nutter obtains from his inviscid model of secondary separation. However, as we have noted in Section 1, the pressure distributions predicted by the inviscid secondary-separation model of Nutter are wholly unrealistic. The displacement effect associated with the flow separation is well illustrated by the displacement function

$$\delta(\theta) = f(\theta)/v_e(\theta) = \int_0^\infty \left(1 - \frac{v}{v_e}\right) \mathrm{d}\zeta \,. \tag{4.1}$$

For the case under consideration Fig. 11 shows this displacement function, which clearly defines the region of strong interaction.

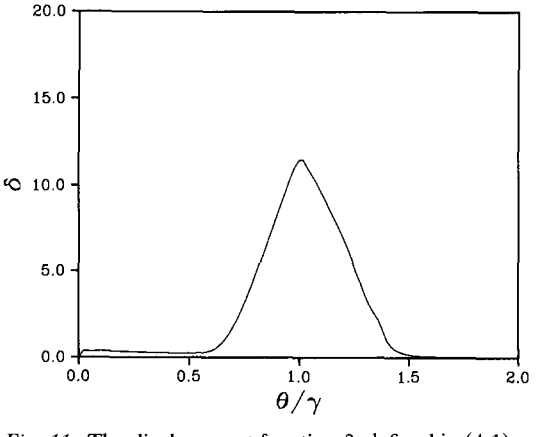

Fig. 11. The displacement function δ, defined in (4.1), following the tenth global iteration; $a = 1$, $\mathrm{Re}_r = 5 \times 10^4$.

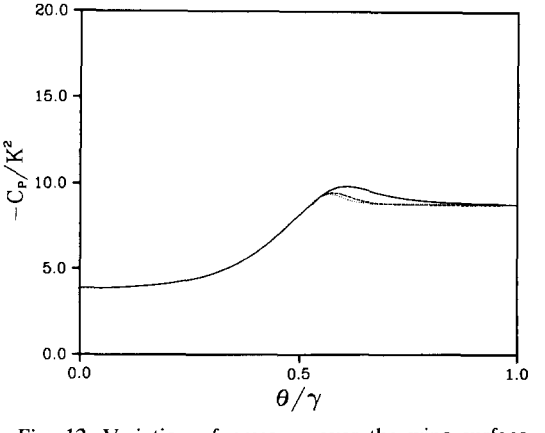

Fig. 12. Variation of pressure over the wing surface with Re_r. (——) $\mathrm{Re}_r = 5 \times 10^3$, (-----) $\mathrm{Re}_r = 5 \times 10^4$, (. . . . .) $\mathrm{Re}_r = 2 \times 10^5$; $a = 1$.

With the incidence parameter $a = 1$ we have also obtained solutions in the Reynolds number range $5 \times 10^3 \leqslant \mathrm{Re}_r \leqslant 2 \times 10^5$. The pressure distributions at the extremities of this range are shown in Fig. 12. We remark that for $\mathrm{Re}_r \geqslant 10^4$, in this range, the pressure distributions are virtually identical. Also we have observed that only towards the lower end of this range does the separation line begin to move outboard from the value $\theta/\gamma = 0.679$. Of course, as Re_r decreases further, the line of separation will move towards the leading edge as the region of separated flow disappears altogether. Similarly the position of the isolated vortex core is relatively unaffected by variations of Reynolds number in this range. In Table 1 we show the position of the separation line and isolated vortex as a function of Reynolds number Re_r. The displacement function δ, defined in (4.1), does increase dramatically with Re_r. However, when this quantity is scaled with $\mathrm{Re}_r^{-1/2}$ (refer to (2.13) for the definition of ζ) then it too is virtually insensitive to variations with Reynolds number in this range. Although it does diminish at smaller values of Re_r, as is to be expected since the separated flow region will eventually disappear.

The above results prompt the following two remarks. First, for Reynolds numbers $\mathrm{Re}_r \geqslant 10^4$ all the flow properties that we have discussed above behave in a conical fashion in the range of Re_r under consideration. In spite of our procedures this is not a result which we may necessarily have anticipated. Second, consider the displacement function δ. What we have demonstrated is that the quantity $\int_0^\infty (1 - v/v_e)\,\mathrm{d}z' = C\hat{r}'$ where, in the range of Re_r considered, C is essentially independent of Re_r. Not only does this confirm the conical nature of the displacement function in physical variables, but it also has implications for an inviscid model of secondary separation of the type considered by Nutter. The vortex, springing from the wing surface, which represents the secondary separation phenomenon in Nutter's model, would be subsumed by the thick separated viscous layer that we have described above. Furthermore if, as our results suggest, this region does not decrease in thickness as the Reynolds number increases, then it seems that Nutter's inviscid model can never be the appropriate limiting flow at high Reynolds number.

We have extended the range of solutions obtained by considering the effects of incidence variation at $\mathrm{Re}_r = 5 \times 10^4$. In particular we have obtained solutions for the four values of the incidence parameter $a = 0.5(0.5)2.0$. For $a = 1.5$, 2.0 the solutions were obtained in a perfectly straightforward manner. However, with $a = 0.5$ difficulties were encountered. These arise, in part, from the fact that the inviscid-flow attachment line no longer coincides with the wing centre-line, and indeed moves slightly following each global iteration. An additional difficulty is that the vortex configuration is now very close to the wing. Care has to be taken that the length of the sheet is such that it does not interfere with the wing, and yet that it is of sufficient length to accommodate the source distribution. We have overcome these difficulties, in part by employing under-relaxation on the flow variables.

Results which we have obtained by varying a are shown in Figs 13 and 14. The pressure variations over the wing surface are shown in Fig. 13. As with the case $a = 1$ the characteristic features of these are that the suction peak is reduced, when compared with the inviscid flow solutions in the absence of secondary separation, and that beyond the

Table 1. Position of the separation line θ_s/γ, and isolated vortex core as functions of Re_r; $a = 1$

Re_r	θ_s/γ	Z_V
5×10^3	0.778	0.636 + 0.284i
5×10^4	0.679	0.637 + 0.280i
2×10^5	0.652	0.636 + 0.278i

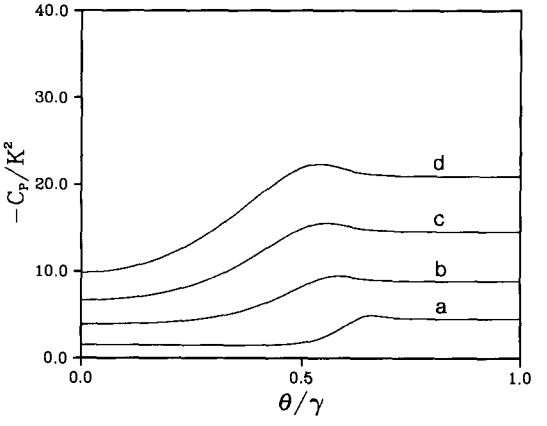

Fig. 13. The variation of pressure over the wing with incidence parameter a. (a) 0.5, (b) 1.0, (c) 1.5, (d) 2.0; $Re_r = 5 \times 10^4$.

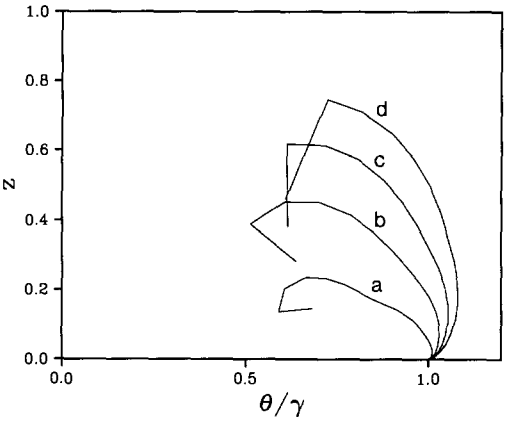

Fig. 14. The sheet shapes for various values of the incidence parameter a. (a) 0.5, (b) 1.0, (c) 1.5, (d) 2.0; $Re_r = 5 \times 10^4$.

separation point there is only a minimal pressure recovery. The position of the separation line itself is shown in Table 2. Woodson and DeJarnette [6] have also carried out calculations for $a = 1.5$ on a wing with $\gamma = 14°$. The separation line is determined from a direct boundary-layer calculation as $\theta/\gamma = 0.7$ which may be compared with our value of 0.657. The sheet shapes for this range of the incidence parameter are shown in Fig. 14. Again, as noted for the case $a = 1$, the isolated vortex core is displaced inboard and upwards by the separated flow region.

Some of the flow features we have presented above may be compared with experiment. Detailed spanwise pressure distributions are presented by Hummel [3] and Marsden et al. [2] for wings with $\gamma = 14°$, 20° and Reynolds numbers based on chord of 9×10^5 and 8×10^5 respectively. These exhibit similar features to the distributions shown in Fig. 13 in the sense that as we move outboard beyond the position of peak suction there is not the significant pressure recovery predicted by a purely inviscid theory. However close to the leading edge another small suction peak is observed, which is indicative of a turbulent re-attachment of the flow. This is confirmed from oil-flow observations. In our model, which is based upon a laminar flow, the separated flow region extends beyond the leading edge. The measured pressures exhibit no conical flow features, as is clear from Hummel's presentation of the streamwise variation of pressure along the wing surface. Over the forward part of the wing the suction values are higher than we have predicted in Fig. 13, and fall in the streamwise direction to the trailing edge where they are lower than our predictions. Although the measured pressure variations are not conical, geometric features of the real flows, which include the separation line, the vortex sheet and the vortex core are remarkably conical. For $a = 1.5$ Hummel finds $\theta_s/\gamma = 0.67$ whilst for $0.5 \leq a \leq 0.75$ Marsden et al. measure

Table 2. Position of the separation line θ_s/γ as a function of the incidence parameter a; $Re_r = 5 \times 10^4$

a	θ_s/γ
0.5	0.730
1.0	0.679
1.5	0.657
2.0	0.651

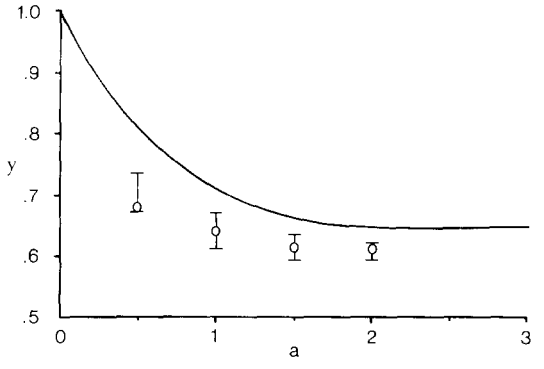

Fig. 15a. A comparison of the vortex core lateral position with experiment. (——) the inviscid solution of Smith [1], o present calculations; $Re_r = 5 \times 10^4$. The bars I denote the range of the experimental results adapted from Lowson [15]. In the experiments Reynolds numbers varied from 10^4 to 7×10^4.

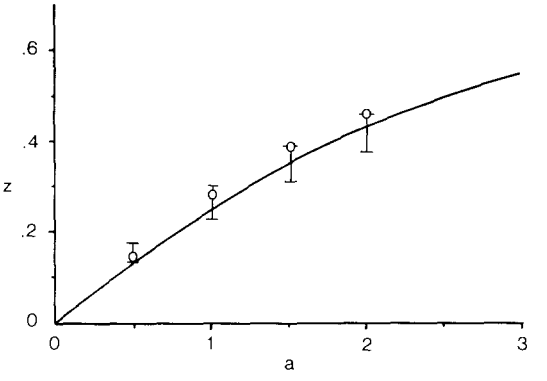

Fig. 15b. As Fig. 15a but for the height of the vortex.

$\theta_s/\gamma = 0.66$. These values may be compared with our calculated values in Table 2. Lowson [15] has provided a useful correlation of vortex core positions from no fewer than ten investigations, which include both laminar and turbulent flow. Our Fig. 15 is adapted from his Fig. 2, which shows the experimental results in more detail. There is general agreement that the effect of the secondary separation is to move the vortex core both upward and inboard. That our results are consistent with this may be seen from Fig. 15.

We may conclude that our model of the secondary separation phenomenon, based as it is upon a fully interactive viscous-inviscid flow, is superior to those which rely upon inviscid vortex-sheet models, of the type discussed by Nutter [4]. However whilst geometric features of the flow, such as the position of the separation line and vortex-core positions, are predicted satisfactorily we can record only qualitative agreement between the measured and calculated pressure distributions.

Appendix

A1. Source-vortex sheet condition

In order to apply the sheet conditions (2.6a,b) and (2.8) for use in the inviscid flow model they are combined in the form of equation (3.2) as follows.

First we express the potential difference $\Delta\Phi$, *at a point on the sheet*, from the equation $g^*(\sigma^*) = -\mathrm{d}\Delta\Phi/\mathrm{d}\sigma^*$ to give

$$\Delta\Phi = \Gamma + \int_{\sigma^*}^{\sigma^*_{\max}} g^*(s)\,\mathrm{d}s\,. \tag{A.1}$$

We next determine the mean values of the tangential and normal velocity components at this point, Φ_{σ_m} and Φ_{n_m} respectively, from

$$\left.\frac{\mathrm{d}W}{\mathrm{d}\sigma}\right|_{\text{sheet}} = \Phi_{\sigma_m} - \mathrm{i}\Phi_{n_m} = \mathrm{e}^{\mathrm{i}\psi^*}\left|\frac{\mathrm{d}Z^*}{\mathrm{d}Z}\right|\left|\frac{\mathrm{d}W}{\mathrm{d}Z^*}\right|_{\text{sheet}}, \tag{A.2}$$

where we have used $dZ^*/d\sigma^* = e^{i\psi^*}$, equation (3.1), $d\sigma^*/d\sigma = |dZ^*/dZ|$, equation (2.11), and again interpret the integrals which appear in dW/dZ^* as Cauchy principal values when evaluated on the sheet. We finally note that, from (2.6a,b)

$$\Phi_{n_m} = -r \sin \phi + \tfrac{1}{2} v_N \,. \tag{A.3}$$

If we now substitute for $\Delta\Phi$, Φ_{σ_m} and Φ_{n_m} from (A.1), (A.2) and (A.3) respectively, in equation (2.8) we obtain the so-called 'pressure-stream surface condition' as

$$-g^*(\sigma^*)\, e^{i\psi^*} \left|\frac{dZ^*}{dZ}\right|^2 \left(\bar{Z}\,\frac{dZ}{dZ^*} - \frac{dW}{dZ^*}\right) + \frac{i}{2}\, g^*(\sigma^*) \left|\frac{dZ^*}{dZ}\right| v_N - \tfrac{1}{2} v_N^2 = \Gamma + \int_{\sigma^*}^{\sigma^*_{\max}} g^*(s)\, ds \,.$$

where we have used $r\, e^{i\phi} = \bar{Z}\, e^{i\psi}$ and $dZ/d\sigma = e^{i\psi}$.

A2. Evaluation of the velocity field

The evaluation of the surface velocities u_e, v_e on the wing, and on the sheet, necessitates the calculation of Φ_x, Φ_y and Φ_z. The velocity components in the y- and z-directions are immediately obtained from the complex velocity as

$$\Phi_y - i\Phi_z = \frac{dW}{dZ} = \frac{dZ^*}{dZ}\,\frac{dW}{dZ^*} \,, \tag{A.4}$$

with dW/dZ^* as in (2.12). The component of velocity parallel to the wing centreline, Φ_x, is now obtained for our conical flow from Euler's theorem on homogeneous functions as

$$\Phi_x = \frac{1}{x}\,(\Phi - y\Phi_y - z\Phi_z) \,, \tag{A.5}$$

where $\Phi = \mathcal{R}e(W)$. To calculate Φ we integrate equation (2.12) to give

$$\begin{aligned} W = {} & -iaZ^* + \frac{\Gamma}{2\pi i} \log\left(\frac{Z^* - Z_V^*}{Z^* + \bar{Z}_V^*}\right) + \frac{1}{2\pi i} \int_0^{\sigma^*_{\max}} g^*(s) \log\left(\frac{Z^* - Z^*(s)}{Z^* + \bar{Z}^*(s)}\right) ds \\ & + \frac{1}{\pi i} \int_0^{t} v_N \left|\frac{dt}{dt^*}\right| \log\left(1 - \frac{Z^*}{t^*}\right) dt^* \\ & + \frac{1}{2\pi} \int_0^{\sigma^*_{\max}} v_N \left|\frac{dZ}{dZ^*}\right| \log\{(Z^* - Z^*(s))(Z^* + Z^*(s))\}\, ds \,. \end{aligned} \tag{A.6}$$

In the evaluation of (A.6) special care must be taken in the evaluation of the logarithmic function. In so doing we note that the path of integration used to derive (A.6) from (2.12) must not cross either the finite part of the source-vortex sheet or the cut which joins its free end Z_E to the isolated vortex Z_V. As with the complex velocity, the third and last terms in (A.6) are evaluated by Simpson's rule, whilst for the fourth term a Gaussian 5-point integration formula is used for computational convenience.

We remove any ambiguity in the determination of the logarithmic function in (A.6) as follows. We denote by Log Z that value of log Z for which the imaginary part exceeds $-\pi$ but is less than π. Suppose we wish to evaluate W on the wing surface, that is on the

imaginary axis in the Z^*-plane, then we have

$$\left.\begin{aligned} &\text{for } \mathcal{I}m(Z^*) \geqslant \mathcal{I}m(Z^*(\sigma^*)), \quad \log(Z^* - Z^*(\sigma^*)) = \mathrm{Log}(Z^* - Z^*(\sigma^*)), \\ &\text{for } \mathcal{I}m(Z^*(\sigma^*)) > \mathcal{I}m(Z^*) \geqslant 0, \quad \log(Z^* - Z^*(\sigma^*)) = \mathrm{Log}(Z^* - Z^*(\sigma^*)) + 2\pi \mathrm{i}, \end{aligned}\right\} \tag{A.7a,b}$$

with similar interpretations for $\log(Z^* - Z_V^*)$ and the logarithm in the fourth term of (A.6).

With Φ_x, Φ_y and Φ_z determined from equations (A.4) and (A.5), the surface velocities on the wing in polar coordinates, namely (u_e, v_e), are evaluated from (2.16a,b).

For the corresponding velocity components on the sheet we use a slightly different procedure. This is because the evaluation of $\mathrm{d}W/\mathrm{d}Z^*$ at a point on the sheet yields mean values of the tangential and normal velocities, Φ_{σ_m} and Φ_{n_m} respectively as in (A.2), thus

$$\frac{\mathrm{d}W}{\mathrm{d}\sigma} = \Phi_{\sigma_m} - \mathrm{i}\Phi_{n_m}. \tag{A.8}$$

To calculate Φ_y and Φ_z on the inner surface of the source-vortex sheet we have

$$\left.\begin{aligned} \Phi_{y_i} &= \Phi_{\sigma_i} \cos\psi - \Phi_{n_i} \sin\psi, \\ \Phi_{z_i} &= \Phi_{\sigma_i} \sin\psi + \Phi_{n_i} \cos\psi, \end{aligned}\right\} \tag{A.9a,b}$$

where the subscript i denotes the inner surface of the sheet. We determine the quantities Φ_{σ_i} and Φ_{n_i} from

$$\left.\begin{aligned} \Phi_{\sigma_m} &= \tfrac{1}{2}(\Phi_{\sigma_i} + \Phi_{\sigma_o}), \\ \Phi_{\sigma_i} - \Phi_{\sigma_o} &= -g(\sigma), \end{aligned}\right\} \tag{A.10a,b}$$

and

$$\Phi_{n_i} = -r \sin\phi + v_N$$

where a subscript o denotes the outer surface of the sheet. Finally, from (A.5) with $x = 1$ (see (2.3)), we have

$$\Phi_{x_i} = \Phi_i - y\Phi_{y_i} - z\Phi_{z_i}, \tag{A.11}$$

and the surface velocities (u_e, v_e) are obtained from (2.17), (2.18).

Acknowledgements

This work was carried out with the support of the Procurement Executive, M.o.D. Helpful discussions with Mr. J.H.B. Smith of the Royal Aerospace Establishment, Farnborough, are gratefully acknowledged.

References

1. J.H.B. Smith, Improved calculations of leading-edge separation from slender delta wings. *Proc. R. Soc.* A306 (1968) 67–90.
2. J.E. Marsden, R.W. Simpson and W.J. Rainbird, An investigation into the flow over delta wings at low speeds with leading edge separation. C.O.Ae., Cranfield Rept. No 114 (1958) 43 pp.
3. D. Hummel, Experimentelle Untersuchung dreidimensionaler laminarer Grenzschichten an einem schlanken Deltaflügel. *Zeits. Flug. Welt.* 10 (1986) 133–145.
4. J. Nutter, *Ph.D. Thesis*. University of East Anglia (1979).
5. D.H. Thompson, Visualization of separated flows in a water tunnel. Australian Defence Scientific Service (1971) Tech. Memo. ARL/A.266.
6. S.H. Woodson and F.R. DeJarnette, A direct and inverse boundary layer method for subsonic flow over delta wings. NASA Conference Publication 2416 (1986) 115–133.
7. A.E.P. Veldman, A numerical method for the calculation of laminar, incompressible boundary layers with strong viscous-inviscid interaction. NLR TR 79023U (1979) 48 pp.
8. N. Riley, Separation from a smooth surface in a slender conical flow. *J. Engng Math.* 13 (1979) 75–91.
9. S.N. Brown, Singularities associated with separating boundary layers. *Phil. Trans R. Soc.* A257 (1965) 409–444.
10. D. Catherall and K.W. Mangler, The integration of the two-dimensional laminar boundary-layer equations past the point of vanishing skin friction. *J. Fluid Mech.* 26 (1966) 163–182.
11. V.V. Sychev, On laminar separation. *Mekhanika Zhidosti i Gaza* 3 (1972) 47–59.
12. F.T. Smith, The laminar separation of an incompressible fluid streaming past a smooth surface. *Proc. R. Soc.* A356 (1977) 443–463.
13. J.E. Barsby, Calculations of the effects of blowing from the leading edges of a cambered delta wing. ARC R & M 3800 (1978) 51 pp.
14. H.B. Keller, A new difference scheme for parabolic problems. In: J. Bramble (ed.), *Numerical Solution of Partial Differential Equations*. New York: Academic Press (1970).
15. M.V. Lowson, Visualization measurements of vortex flows. AIAA Paper-89-0191, 27th Aerospace Sciences Meeting Reno 1989, 10 pp.